Impact of Active Turbulence Generation System in 3/4 Open-Jet Wind Tunnel: Flow Structures, Shear Layer, and Low-Frequency Fluctuations

Qing Jia [1,2], Lanwei Qin [1,2], Civil Zhao [1,2], Yikun Wang [1,2], Chao Xia [1,2,3], Zhigang Yang [1,2], Huanxia Wei [1,2,4,*],

1 School of Automotive Studies, Tongji University. **2** Shanghai Key Lab of Vehicle Aerodynamics and Vehicle Thermal Management Systems, Tongji University. **3** Department of Mechanics and Maritime Sciences, Chalmers University of Technology. **4** Department of Mechanical Engineering, National University of Singapore.

Corresponding Author. Email address: huanxia.wei@u.nus.edu

Abstract

With increasing attention to complex aerodynamic conditions such as crosswinds, gusts, road turbulence, and vehicle drafting, accurately reconstructing these unsteady and turbulent environments in automotive wind tunnels has become a significant challenge. Addressing this challenge is crucial for broadening experimental conditions and advancing research in unsteady aerodynamics. However, the integration of turbulence generation systems impacts low-frequency fluctuation phenomena, leading to pressure and velocity inaccuracy, and also affects the flow structure in the test section as well, especially in the jet shear layer. In this paper, the impact of an active turbulence generation system on turbulence characteristics and flow structures within jet shear layer in a wind tunnel is numerically investigated. By comparing the flow structure among the empty wind tunnel, and wind tunnel with static and dynamic active turbulence generation system, the mechanisms underlying these configurations are analyzed. In addition, low-frequency fluctuations with the presence of active turbulence generation system are compared to those observed in the empty wind tunnel. The results indicate that while the turbulence generation system effectively produces the desired turbulent components, it also increases the non-uniformity of the jet shear layer, and hence intensifies low-frequency fluctuations in the test section.

Keywords: Turbulence generation system, low-frequency fluctuations, wind tunnel, shear layer

Introduction

With advancements in computational fluid dynamics (CFD) and wind tunnel testing technologies, there is increasing interest in understanding the aerodynamics of vehicles under real road flow conditions. Factors such as the presence of road obstacles, wake of other vehicles, and the inherent instability of natural wind contribute to turbulent aerodynamic conditions on the road. As a result, vehicles are frequently subjected to unsteady airflow patterns during actual driving.

In wind tunnels, reconstructing road turbulence typically involves the use of turbulence generation systems, which can be classified into passive and active devices. Passive systems often use fixed structures, such as turbulence grids or triangular vortex units positioned near the nozzle or contraction section in the wind tunnel. For instance, McAuliffe et al. designed the Road Turbulence System (RTS) featuring a spire-based passive turbulence generator. They compared the generated turbulence components with results from real world road tests and found that the system could effectively reconstruct road turbulence according to the turbulence intensity, length scale, and frequency spectral distribution [1]. Similar designs are also commonly used in wind tunnels for testing buildings together with friction units on the ground in the test section, to reconstruct the wind properties in the atmospheric boundary layer.

While passive turbulence generators are relatively simple to implement, they offer limited control over turbulence characteristics. Sharp edges on these devices can also introduce undesirable high-frequency transition noise, which interferes with acoustic measurements. Moreover, the turbulence scale necessary to simulate unsteady road flow is often significantly larger than what passive devices can produce. Generating turbulence at scales larger than the test vehicle using passive grids is impractical, prompting researchers to explore active turbulence generation systems.

Active turbulence generation systems can be categorized based on how they manipulate the flow, either through resistance or lift. Neuhaus et al. designed an active diamond-shaped grid that generates turbulence with length scales significantly larger than the width of the wind tunnel through its motion [3]. Cogotti et al. developed a resistance-based active turbulence generator capable of reconstructing real road flow conditions in the wind tunnel. By adjusting the opening angle of the generation unit, the turbulence intensity and scale could be well controlled. Additionally, by changing the relative positions of different sections, it also has the capacity to simulate dynamic crosswind and gust conditions while driving [4-6].

Lift-based active devices, on the other hand, typically use vertically controlled deflectors installed upstream in the test section. An early design by Schröck et al. featured four deflectors, each half the height of the nozzle, to generate turbulence in the wind tunnel [7]. This design was later refined by Blumrich et al. for the FKFS wind tunnel at the University of Stuttgart, namely FKFS Swing system, which is used to study road turbulence and crosswind [8-9]. Mankowski et al. designed a system using two vertical deflectors at the nozzle, which further reduces the impact on airflow uniformity at the center of the wind tunnel nozzle [10].

A common issue in 3/4 open-jet automotive wind tunnels is low-frequency fluctuations [11-12]. These fluctuations result from the formation of vortex shedding structures at the nozzle, which propagate downstream with the airflow. When these vortical structures interact with the collector at frequencies coinciding with the tunnel's natural modes, the resonance-like phenomenon occurs, causing significant pressure and velocity fluctuations throughout the test section. Such low-frequency fluctuations not only compromise the accuracy of flow field measurements but also impose hazardous loads on the wind tunnel structure due to the resulting oscillations [13]. Therefore, understanding the impact of low-frequency fluctuations when

designing and employing active turbulence generation systems in the wind tunnels is significant.

Related work on low-frequency fluctuations dates back to the 1990s when the American Institute of Aeronautics and Astronautics (AIAA) investigated the interaction between nozzle vortex shedding and the collector. This interaction, referred to as the "Edgetone-Type Feedback" effect, was first described by Bartel and McAvoy [14-15], who extended the Rossiter formula to establish a practical semi-empirical relationship between the frequency of large vortex structures in the jet shear layer and the flow velocity [16]. This formula has since been widely used to predict the dominant frequency of low-frequency fluctuations in automotive wind tunnels. Building on the Rossiter formula, Zheng et al. examined modes generated at different wind speeds in a model wind tunnel, successfully predicting the primary frequency of these fluctuations [17]. Bao et al. further investigated the flow mechanisms behind the interaction between the jet shear layer and the collector, demonstrating how a simple vortex generator effectively suppresses low-frequency fluctuations [18]. During an upgrade of the full-scale aeroacoustic wind tunnel at FKFS, Wiedemann et al. designed and implemented the FKFS Besst vortex generator to reduce low-frequency fluctuations, with subsequent studies providing detailed analyses of its performance [8-9]. Additionally, Jia et al. demonstrated that using an acoustic synthetic jet actuator to actively control nozzle jets effectively suppresses low-frequency fluctuations in model wind tunnels by disrupting vortex shedding at the nozzle, thereby improving the flow field quality [19].

In modern wind tunnel construction, accurately reconstructing real-road conditions is essential for expanding the capabilities of aerodynamic testing. Current active turbulence generation provide basically precise control over turbulence characteristics such as turbulence intensity, length scale, spectral distribution, and simulate both steady and unsteady crosswind conditions. However, despite significant advancements in turbulence generation, few studies have focused on the impact of these systems on low-frequency fluctuations in wind tunnels. Therefore, how active turbulence generation devices affect the low-frequency fluctuations and flow structures in the shear layer is still a research gap.

Methodology

To investigate the turbulence characteristics, modifications in the jet shear layer flow structure, and the effects on low-frequency fluctuations by the active turbulence generation system, a 1:15 scaled model wind tunnel from Shanghai Automotive Wind Tunnel Center (SAWTC) was utilized in this study, and more details could be referred from our previous work [20]. The fluid region of the wind tunnel includes the contraction section, nozzle, breathers, plenum chamber, collector, diffuser, and an extended diffuser section (Figure 1).

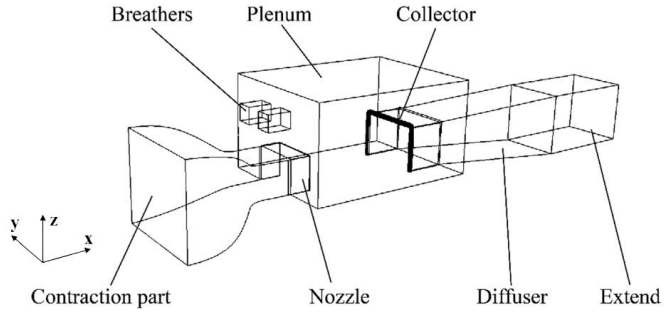

Figure 1. Sketch of the wind tunnel without turbulence generation system.

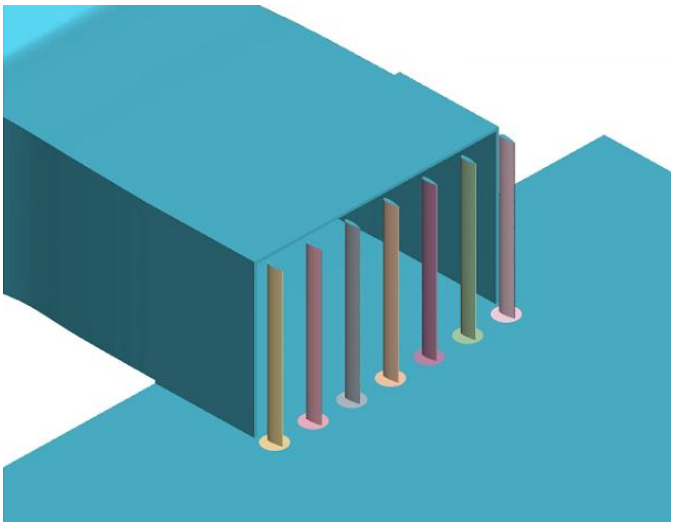

Figure 2. Geometry of the active turbulence generation system.

As the primary objective is to evaluate the impact of the turbulence generation system on the flow field and low-frequency fluctuations, a standard NACA0020 airfoil was selected for the deflector blades in the system with the purpose of minimizing experimental variability. The geometric parameters of the airfoil were determined according to the dimensions of the wind tunnel model. The NACA0020 airfoil features a chord length of 27 mm, with its rotation center located at 44% of the chord length. The maximum thickness, which is 20% of the chord, is positioned at 29.7% of the chord. In our previous study, configurations with 6 and 7 deflectors were compared, and the results indicated that a 7-deflector configuration provided a more compact layout, allowing for higher energy input with shorter actuation strokes [21]. Following this conclusion and drawing on the setup used in the FKFS wind tunnel at the University of Stuttgart, seven NACA0020 airfoils were symmetrically arranged along the centerline of the wind tunnel, with a spanwise spacing of 60 mm between neighboring deflectors. To isolate the effects of the airfoils on the jet shear layer and eliminate potential interference from the actuators, the geometry for simulations was designed without actuators. The final arrangement of the active turbulence generation system at the nozzle in the wind tunnel is shown in Figure 2.

The reference turbulence intensity and length scale collected by McAuliffe et al. during the design of the Road Turbulence System (RTS) are summarized in Table 1. They were obtained under typical road conditions by a real SUV equipped with sensing system, characterized by moderate terrain roughness, medium traffic density, and moderate wind speed. This data serves as the baseline for evaluating wind tunnel turbulence conditions, ensuring a standardized and comparable turbulence environment. The turbulence values were normalized to be compatible with the 1:15 scale model wind tunnel used in this study.

Table 1. Turbulence intensity and normalized turbulence length scale from road measurements [1].

Direction	Turbulence intensity I	Normalized turbulence length scale L^x
u	4.0 %	0.31 m
v	3.5 %	0.13 m
w	3.1 %	0.04 m

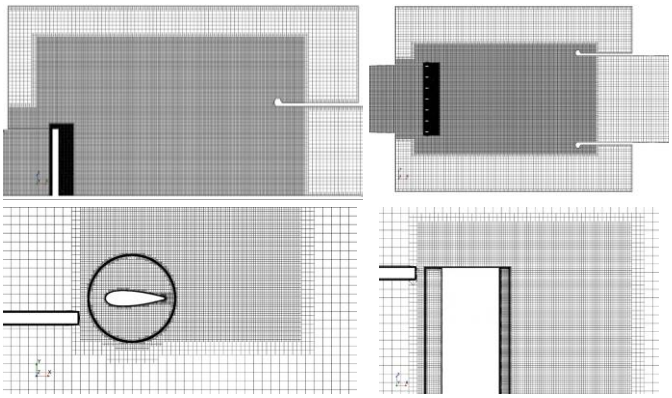

Figure 3. Mesh distribution in the computational region.

The simulations studied were performed based on STAR-CCM+, a commercial CFD platform. The steady state of simulation is performed using the Realizable K-epsilon model with all y^+ wall treatment, and after the convergence of the steady simulation, the steady results are defined as the initial condition for the unsteady simulation, during which, the Large Eddy Simulation (LES) model was employed, along with wall-adapting local eddy-viscosity (WALE) subgrid-scale model, and all y^+ treatment. The convection and diffusion terms are in boundary-centered difference scheme and second-order upwind discrete scheme, respectively. The mesh distribution is shown in Figure 3, using a 12 mm trimmed cell with 10-layer prism layer, a growth rate of 1.1. The sizes of the refined grid regions range from 3 mm to 1.5 mm to 0.75 mm, with a transition grid of 6 mm between the coarse and fine grids. In regions near the airfoils, where flow separation is expected, the grid size is further refined to 0.75 mm. Finally, the total number of mesh is 44.5 million, and the mesh reliability is validated by a series of convergence check, which could be found in our previous study [20]. Velocity inlet before the contractor is applied, while the other side employs a pressure outlet with higher relaxation factor after the extension section after diffuser.

The maximum operating frequency is 5 Hz due to the physical loading requirements of mechanical structures, especially the performance of preferred motor. To take flow separation caused by the deflector airfoils and the influence of low-frequency fluctuations into consideration, the maximum deflection angle is set at 12°. The rotation of the deflectors is implemented using rigid body motion (RBM) scheme, with the incoming velocity of 25 m/s, which is exhibiting high sensitivity to low-frequency fluctuations, and hence the bulk Reynolds number is 5.7×10^5. The collector angle is maintained at 0°, as low-frequency fluctuations are most pronounced at this angle.

Data acquisition begins after the convergence of the unsteady simulation, with a sampling frequency of 1000 Hz and a total sampling duration of 1.0 second. Thirteen measurement points are positioned in the test section for velocity and pressure data acquisition, as shown in Figure 4. Of these, six streamwise measurement points are located at the intersection of the nozzle centerline height and the vertical symmetry plane, spaced 100 mm apart, with the first point (Point 1) positioned 100 mm from the nozzle. Four spanwise measurement points are arranged along the nozzle center height plane, spaced 50 mm apart, all placed on one side due to the nozzle's symmetry. Additionally, five vertically arranged measurement points are located on the vertical symmetry plane, spaced 50 mm from the nozzle center height plane.

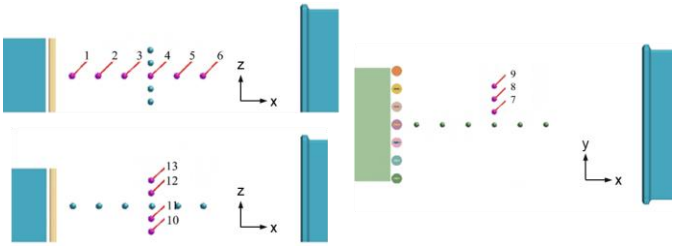

Figure 4. Arrangement of measurement points in the test section.

For simulation feasibility verification, the wind tunnel used in the numerical simulation of this study corresponds to the 1:15 scaled automotive model wind tunnel at SAWTC. Wang et al. conducted a comparative study between the simulation and experimental results of the original nozzle in this model wind tunnel. By analyzing the surface pressure data at the test points, it was found that the pressure spectrum from the simulation matches with experimental measurements, confirming the validity of the simulation method used in this study [20].

Results and Discussion

In this section, numerical results are presented in detail, followed by analysis and discussion of the flow field based on these results. First, the averaged field is discussed to understand the impact of the presence and operation of the turbulence generation system on the flow field structure and airflow quality. Then, proper orthogonal decomposition (POD) is applied to decompose the flow field and obtain the energy and frequency distribution of the dominant modes. Finally, multiple snapshots of transient fields are presented and discussed, with a focus on the vortical dynamics and evolution within the shear layer.

Time Averaged Flow Field

The analysis centers on the non-dimensional size range of the mid-sectional plane, specifically $3.8 < X/D_h < 6.3$ and $-0.413 < Z/D_h < 1.2$. This region includes the main flow area, extending from the nozzle plane to the collector plane and from the bottom of the test section to the upper boundary of the jet shear layer, as illustrated in Figure 5. By concentrating on the flow variations within this region, key changes in the wind tunnel's flow field can be analyzed. In the subsequent study, the original wind tunnel model is referred to as the italicized "*Baseline*," the installation of the turbulence generator without motion as "*Static*," and with motion as "*Dynamic*."

The analysis on time-averaged flow field starts from the turbulence intensities in the streamwise, spanwise, and vertical directions, which are defined as:

$$I_i = \frac{u'_i}{U_i}$$

where u'_i represents the standard deviation of specific velocity component. Turbulence intensity contours, as shown in Figure 6, highlight areas with significant fluctuations, including cases of *Dynamic*, *Static*, and *Baseline*, which are compared to assess the impact of the turbulence generation system on the turbulence properties.

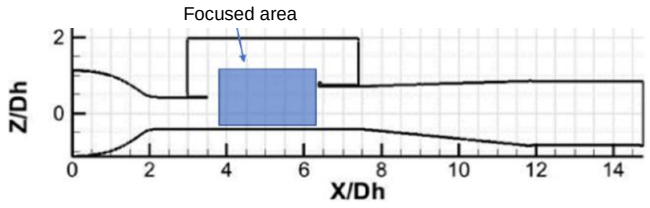

Figure 5. Mid-sectional view of the geometry with non-dimensional coordinate system, with focused area overlayed.

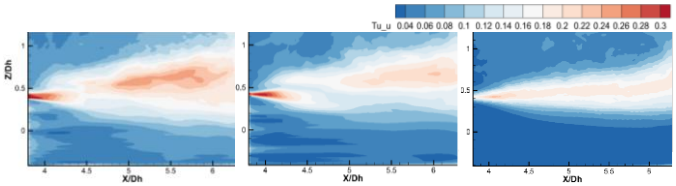

(a) (b) (c)

Figure 6. Streamwise turbulence intensity on x-z mid-section: (a) *Dynamic*, (b) *Static*, and (c) *Baseline*.

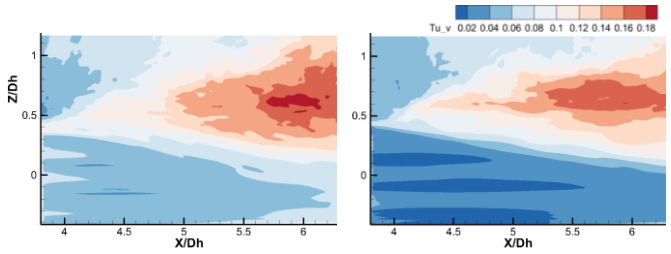

(a) (b)

Figure 7. Spanwise turbulence intensity on x-z mid-section: (a) *Dynamic* and (b) *Static*.

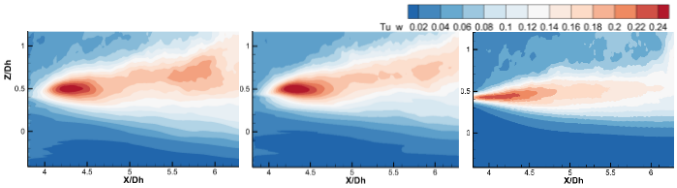

(a) (b) (c)

Figure 8. Vertical turbulence intensity on x-z mid-section: (a) *Dynamic*, (b) *Static*, and (c) *Baseline*.

As for *Dynamic*, the streamwise turbulence intensity in the mid-to-rear section of the jet shear layer increases by approximately 2% compared to *Static*, with values ranging between 20% and 24%. Additionally, at the mid-height of the test section, the turbulence intensity increases by around 2%, from 4% ~ 10% in *Static* to 6% ~ 12% in *Dynamic*. When compared to *Baseline*, the turbulence intensity affected by the turbulence system is notably higher than that produced by the original state. Near the nozzle, jet expansion occurs both inward and outward along the upper edge, while the deflectors of turbulence generation system are aligned with the nozzle height. The interaction between the airflow and the sharp edges of the deflectors induces periodic vortex shedding, which further combined with the vortices from the edge of nozzle, results in changes in turbulence in the test section. This leads to a noticeable increase in streamwise turbulence intensity near the nozzle, especially at the upper trailing edges of the deflectors of turbulence generation system.

The *Static* condition showed spanwise turbulence intensity at the bottom of the test section in the range or 2% ~ 4%, while *Dynamic* operation increased the levels to 6% ~ 8%, both with a relatively uniform distribution throughout the test section (Figure 7). The vertical turbulence intensity contours, shown in Figure 8, reveal no significant impact on the vertical turbulence, whether under the *Dynamic* (5 Hz motion) or *Static* of the turbulence generation system. The magnitude and distribution of turbulence intensity remain almost unchanged. This is because the motion of deflectors primarily affects the streamwise and spanwise turbulence intensities, with minimal influence on vertical velocities. However, compared to *Baseline*, a noticeable concentration of vertical turbulence intensity is observed at X/D_h = 4.3. This phenomenon is attributed to the development of large vortex structures caused by enhanced natural vortex shedding, increasing z-direction velocity fluctuations in this region.

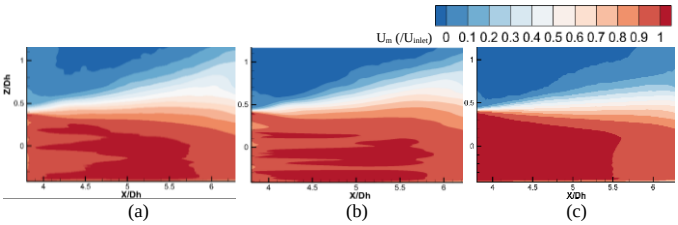

(a) (b) (c)

Figure 9. Streamwise mean velocity on x-z mid-section: (a) *Dynamic*, (b) *Static*, and (c) *Baseline*.

The averaged streamwise velocity distribution normal to y-axis is shown in Figure 9, which is normalized by dividing it by the nozzle flow velocity (25 m/s). The region where 0.1<U<0.9 can be regarded as the jet shear layer. It can be observed that, under *Dynamic*, the shear layer in the downstream half of the test section expands, compressing the area in the potential flow region in the test section. Compared to the *Baseline*, jet shear layer expands slightly more than that without turbulence generation system. The potential flow region of the test section is a critical region where vehicle data measurements are typically conducted, hence its area is always important for testing. After installing the turbulence generation system, the potential flow area (U≥0.9) is compressed. This occurs because the turbulence generation system increases the instability of the jet shear layer, and the formation of large vortices amplifies low-frequency fluctuations. Additionally, the wake of the deflectors is also unstable, and the turbulent components induced by the deflectors further contribute to the velocity pulsations in the test section. Overall, since the primary objective of the turbulence generation system is to induce velocity pulsations to generate specific turbulence in the test section, the resulting non-uniform averaged velocity distribution is reasonable.

Low-frequency Fluctuations and Dynamic Modes

In this subsection, the Proper Orthogonal Decomposition (POD) method is used to decompose the flow field and extract the dominant flow dynamic modes from the temporal data for further analysis. The POD analysis is based on the same focused region, shown in Figure 5, using 1000 transient flow field snapshots at 1000 Hz, to process both pressure and velocity data. By performing FFT spectral analysis on the temporal coefficients of the low-order POD modes, the flow spectral characteristics are analyzed.

The first 20 velocity POD modes are shown in Figure 10, crossing three cases. For Static, the first two modes account for a relatively high proportion of the total energy, at 13.5% and 13.2%, respectively. As the mode order increases, the energy proportion gradually decreases. The third and fourth orders of modes account for 8.2% and 7.1%,

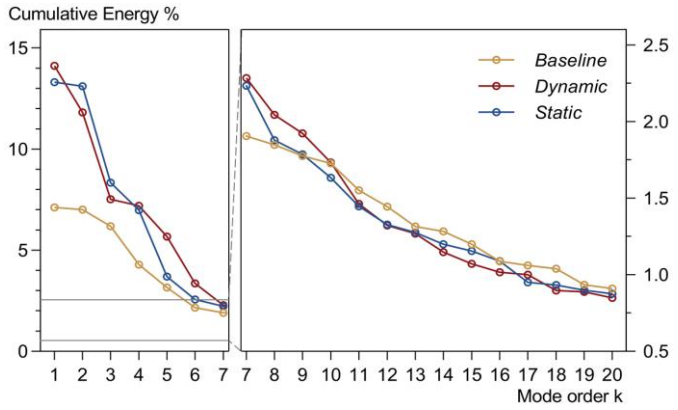

Figure 10. Energy distribution of first 20 orders of velocity POD modes.

respectively. Together, the first four orders of modes represent approximately 42% of the total velocity variation, indicating that the velocity fluctuations are predominantly concentrated in these four modes, and higher-order modes contribute less to mode energy. Therefore, the following analysis mainly focuses on the first four modes. In comparison, the first four velocity modes under *Baseline* show a lower total energy proportion around 24%, and the first two modes account for 7.1% and 7%, significantly lower than *Static*. This indicates that the turbulence generation system induces stronger velocity fluctuations, significantly increasing the energy contribution of the first two modes, with the deflectors playing a crucial role in generating vortex structures and amplifying the fluctuations. When the system is in operation (*Dynamic*), the energy contribution of the first mode increases to 14%, while the second mode decreases to 11.9%, which differs from the *Static* condition where the energy contributions of the first and second modes are nearly identical. Under the *Dynamic* condition, the third and fourth order of velocity modes contribute 7.5% and 7.4%, respectively. The total energy contribution of the first four modes is approximately 41%, about 1% lower than *Static*. This indicates that the velocity disturbances introduced under the *Dynamic* condition reduce the energy proportion of low-frequency velocity fluctuations in *Static*.

The power spectral density (PSD) of the time coefficients from the first four-order velocity POD modes of the three cases are shown in Figure 11. The peak of first mode pair (first and second order) of *Baseline* locates at 21 Hz, whereas that of *Static* exhibit higher frequencies of 40 Hz. For *Static*, the peaks of second mode pair are at 20 Hz. In terms of amplitude, the first mode pair of *Static* has significantly higher amplitudes than that of *Baseline*, while the amplitudes of the second mode pair of *Static* are comparable to the first mode pair of *Baseline*. This indicates that the presence of deflectors introduces higher-frequency and larger-amplitude velocity fluctuations. When taking the motion of deflectors into consideration (*Dynamic*), the primary frequency of velocity fluctuations shifts, comparing to *Static*. The peak frequencies for the first mode pair changes to 20 Hz, while the peak of second mode pair shifts to 40 Hz. This demonstrates that under *Dynamic*, the velocity fluctuations at 20 Hz are relatively amplified, while the 40 Hz fluctuations are relatively weakened. In terms of amplitude, the peak value under *Dynamic* is about 43,000 Pa^2/Hz, while under *Static*, the peak for the first and second modes reaches approximately 48,000 Pa^2/Hz. This suggests that the amplitude of the velocity fluctuations is reduced when the turbulence generation system operates in *Dynamic*. In addition, the spectral energy at peak frequencies has more than a hundred times the variability relative to other frequencies. In most bands, the energy is below 100 Pa^2/Hz. It further demonstrates the hazards of low-frequency fluctuation, especially after introduction of turbulence generation systems.

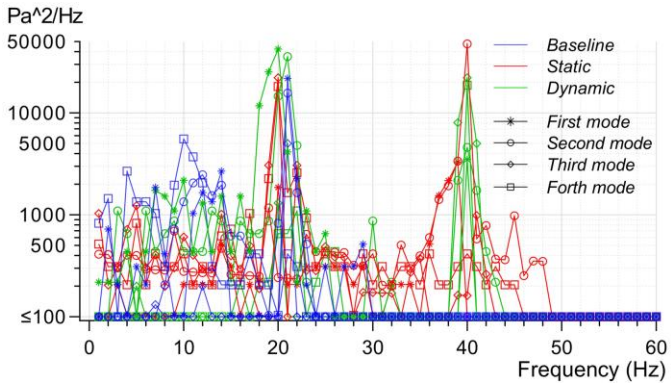

Figure 11. Power spectral density of POD time coefficients from first four velocity modes.

Figure 12 shows the energy distribution of the first 20 pressure POD modes. It can be observed that under *Static*, the energy contribution of the first pressure mode exceeds 80%. In comparison, for *Baseline*, the energy contribution of the first mode is only around 50%. This indicates that deflectors amplify the low-frequency fluctuations, concentrating more energy in the lower modes. The energy distribution of pressure mode under *Dynamic* is almost the same to that of *Static*, suggesting that dynamic operation has minimal impact on the pressure fluctuations. This is because pressure fluctuations are closely related to the breakdown of large vortices in the shear layer. As the motion of system does not significantly alter the vortex structures within the shear layer, which has been discussed before, the corresponding pressure fluctuations remain less changed as well.

Figure 13 presents the PSD for the first four pressure POD modes of *Static* and *Baseline* at low frequency range, and the i^{th} modes of *Static* are labeled as TGS_i. It is shown that, for *Baseline*, the pressure fluctuations in all the first four low-order modes show their peaks at 21 Hz, with amplitudes on the order of 10^7. As for *Static*, the first and second pressure modes occur at 40 Hz, with the amplitude of the first mode being an order of magnitude higher than the peak value observed in the *Baseline*. Furthermore, the third and fourth modes are at 20 Hz, where the amplitudes of the 2-4^{th} pressure modes are basically the same as the peak value in the *Baseline*. This indicates that in the *Static* condition, the flow field exhibits a significant pressure fluctuation at 40 Hz, accompanied by a secondary pressure fluctuation at 20 Hz. From the perspective of vortex structures causing pressure fluctuations, for *Static*, vortex shedding at 40 Hz exhibits a higher energy proportion, while the alternating mode of adjacent vortices caused by vortex evolution accounts for a relatively smaller proportion. It can be deduced that deflectors provide a stabilizing effect on the flow direction, slightly suppressing the mode variability of adjacent two vortices. The detailed vortex dynamics will be discussed in the next subsection.

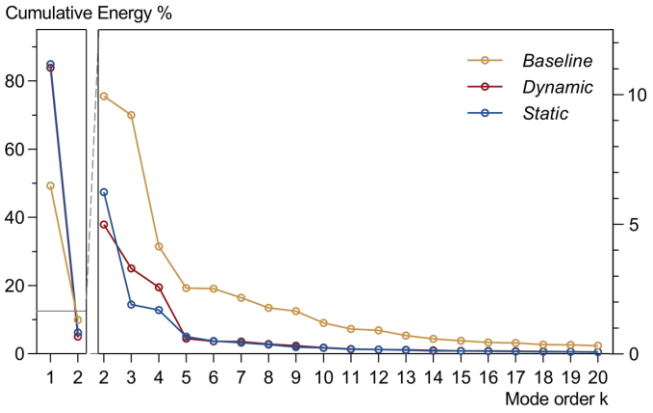

Figure 12. Energy distribution of first 20 orders of pressure POD modes.

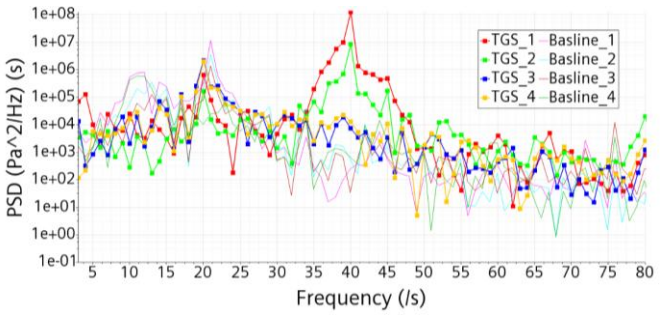

Figure 13. Power spectral density of POD time coefficients from first four pressure modes under *Static* and *Baseline*.

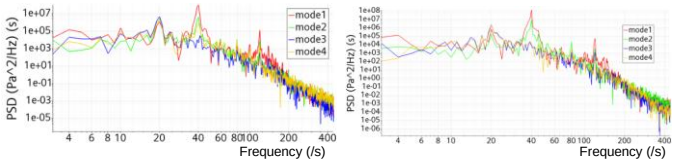

Figure 14. Power spectral density of POD time coefficients from first four pressure modes: (a) *Dynamic*, and (b) *Static*.

Further, the frequency range of interest is expanded, and the operation of the turbulence generation system (*Dynamic*) is taken into consideration, shown in Figure 14. The PSD of the *Dynamic* and *Static* are very similar, with peaks at 40 Hz for the first and second pressure modes, and at 20 Hz for the third and fourth pressure modes. The key difference is that the peaks at 40 Hz and 20 Hz are broader in the *Dynamic* condition, while the peaks in *Static* are sharper. Based on amplitude, the peaks at 40 Hz are slightly lower in *Dynamic*, while the peaks at 20 Hz are larger, compared to *Static*. This suggests that the motion of deflectors slightly spreads out the peak frequency of the pressure fluctuations while amplifying them at lower frequencies.

Regarding the dominant frequency of low-frequency fluctuations in both velocity and pressure, the introduction of the turbulence generation system alters the frequency of vortex shedding and the Rossiter mode excitation in the wind tunnel. The theoretically calculated frequency for the third-order Rossiter mode is 37.727 Hz, but this is also influenced by the changes in the nozzle structure, shifting the vortex-shedding Rossiter mode frequency to about 40 Hz. The combined vortex shedding frequency of 40 Hz and the 20 Hz vortex ring pair motion frequency act as excitations, which are similar to the first and second Helmholtz resonant cavity modes (21.3 Hz and 42.6 Hz) and the third-order duct acoustic mode (39 Hz) of the model wind tunnel. These excitation sources trigger the response modes in the wind tunnel, leading to a strong resonance phenomenon with periodic velocity and pressure fluctuations in the test section.

Unsteady Flow Characteristics

In this subsection, the vortex structures within the shear layer are identified analyzed using Q-criterion contour, which is a commonly used and powerful vortex identification method. The definition of Q-criterion is given by:

$$Q = \frac{1}{2}\left(\sum_{i,j}\Omega_{ij}\Omega_{ij} - \sum_{i,j}S_{ij}S_{ij}\right) \tag{1}$$

where Ω_{ij} is the rotation rate tensor (the antisymmetric part), and S_{ij} is the strain rate tensor (the symmetric part). They are defined as:

$$\begin{cases} S_{ij} = \frac{1}{2}\left(\frac{\partial u_j}{\partial x_i} + \frac{\partial u_i}{\partial x_j}\right) \\ \Omega_{ij} = \frac{1}{2}\left(\frac{\partial u_j}{\partial x_i} - \frac{\partial u_i}{\partial x_j}\right). \end{cases} \tag{2}$$

In this calculation. the sampling frequency for the Q-criterion contour is set at 1000 Hz, covering a period of 0.025 s.

The temporal snapshots of Q-criterion contours of the mid-plane section under Baseline, i.e., the empty wind tunnel, are shown in Figure 15, and the three dominant vortices are labeled as 1, 2, and 3. The vortical structures keep their shape for a relatively long period with the development of jet boundary layer.

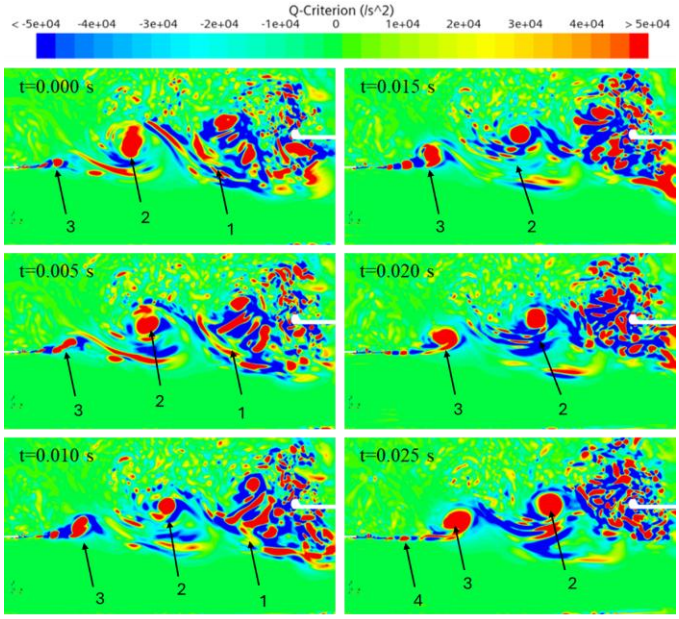

Figure 15. Q-criterion contours of the x-z mid-section for *Baseline*.

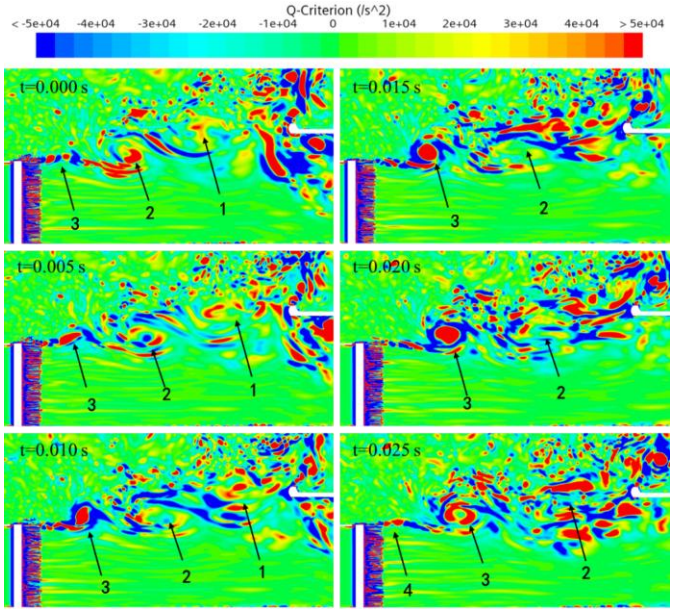

Figure 16. Q-criterion contours of the x-z mid-section for *Static*.

Figure 16 shows the Q-criterion results under *Static*, and numbering of vortices are overlapped as well. In terms of their temporal relationships, these three vortices represent different stages of vortex evolution after shedding from the nozzle. Vortex 1 is the nearest one from the collector. It has a large radius but a low rotational speed, indicating that its energy is highly dissipated during spatial migration, and it is at the final stage of vortex breakdown. From t = 0.005 s onward, it breaks into numerous smaller vortex structures. Vortex 2 is at its most energetic stage, with clear vortex edges. At the same time, the radius of vortex 2 continues to increase, and its rotational speed gradually decreases as energy is dissipated during the vortex merging. By t = 0.020 s, it has broken down into smaller vortices. Vortex 3, on the other hand, represents a newly shed pair of embryonic vortices from the edge of the nozzle, which show clear edges. As they move downstream within the jet shear layer, they absorb energy and grow, repeating the process seen in vortex 1 and 2, including vortex merging, dissipation, and eventual breakdown. Notably, adjacent vortex rings form vortex

pairs, exhibiting different vertical patterns. For instance, vortex ring 1 tends to move upward toward the collector as it breaks down, while vortex 2, influenced by the interactions between vortex 1 and 3, moves downward toward the collector. This flow behavior is similar to the Kármán vortex street, and also results in a secondary fluctuation at 20 Hz, half the shedding frequency.

From Figure 17, in the jet shear layer under *Dynamic*, the development patterns of vortex rings 1, 2, and 3 are essentially the same as those observed under the previously mentioned *Static*. However, some subtle differences are still noted. Specifically, as for *Dynamic*, the vortex structures in the jet shear layer appear more fragmented. The edges of the large vortices are more easily distorted by surrounding smaller vortices, resulting in a more irregular appearance. In contrast, the edges of the large vortices in the *Static* condition are clear, indicating a more spatially concentrated energy distribution. Additionally, at downstream in the jet shear layer, the number of small vortices is relatively greater in the *Dynamic* condition due to disturbances caused by the deflectors, compared to *Static*.

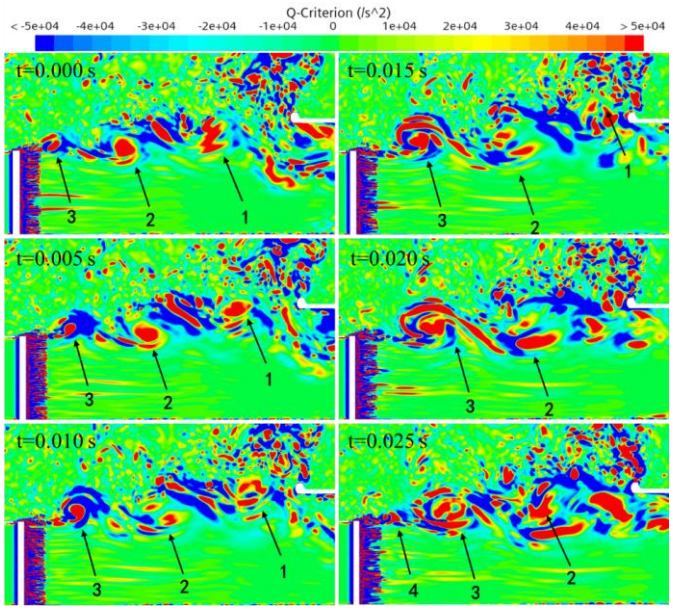

Figure 17. Q-criterion contours of the x-z mid-section for *Dynamic*.

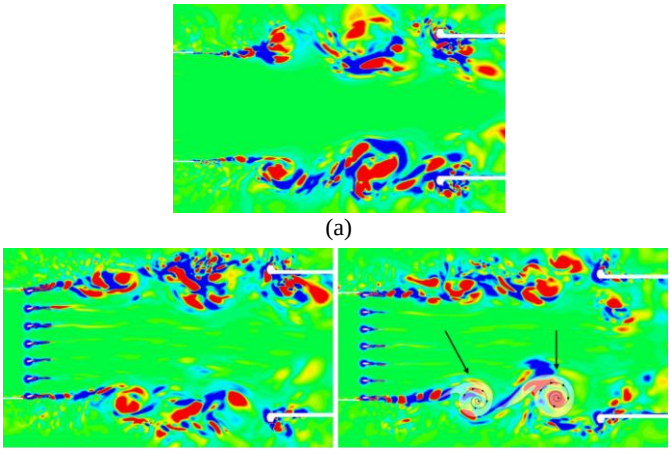

(a)

(b) (c)

Figure 18. Q-criterion contours of x-y mid-section: (a) *Baseline*, (b) *Dynamic*, and (c) *Static*.

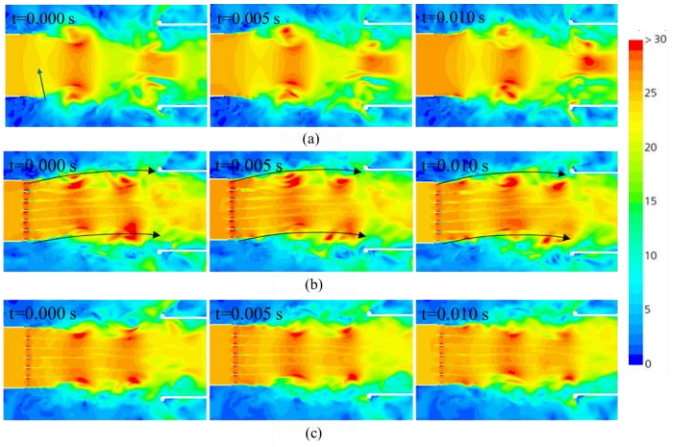

Figure 19. Instantaneous velocity magnitude field of horizontal mid-section: (a) *Baseline*, (b) *Dynamic* and (c) *Static*.

In Figure 18, the horizontal cross-sectional Q-criterion contours at the center height are compared between *Dynamic* and *Static*. The sampling frequency and parameter settings are the same as previously described. For *Static*, two large vortex structures in the jet shear layers are marked, with clearly defined boundaries and discernible movement patterns. However, under *Dynamic* condition, the boundaries of the large vortex structures in the jet shear layer become more irregular. By the time these structures reach the downstream half of the domain, their movement patterns and outlines become difficult to discern. It is suggested that the disturbances caused by the turbulence generation system blur the boundaries of the vortex structures within the jet shear layer, and lead to more chaotic airflow as well. What's more, turbulence in *Baseline* exhibits a simpler shape and enhanced autocorrelation. Figure 19 compares the velocity magnitude distribution at the center height of the nozzle. It is evident that, under the influence of low-frequency fluctuations, velocity periodic pulsations occur in the test section regardless of whether the turbulence generation system is working, with certain flow segments exhibiting velocities exceeding the nozzle velocity. For *Dynamic*, the airflow spanwise deviation caused by the deflectors is clear, as marked with the black curve representing the general flow direction. In contrast, under the *Static* condition, there is no noticeable airflow spanwise deviation, however, low-frequency fluctuations still induce velocity pulsations. A potential reason is that low-frequency fluctuations affect the deflection and spanwise deviation of the airflow. Compared to *Static*, the area of the high-velocity region of *Dynamic* is slightly larger (marked in red), indicating that the velocity pulsations are more distinct when the turbulence generation system is in operation. Comparing to Baseline, the presence of turbulence generation system makes the shear layer thinner, and improves the flow quality in the test section. This may be caused by the interaction of passively (for *Dynamic* and *Static*) and actively (for *Dynamic*) generated turbulence by the deflectors with the flow in the shear layer.

Conclusions

In this paper, the impact of an active turbulence generation system on the jet shear layer and low-frequency fluctuations are numerically studied. A comprehensive analysis of the flow field is conducted focusing on the time-averaged flow field, the spatio-temporal evolution of vortex structures, and frequency of POD dynamic modes as well. By examining the flow field characteristics of the turbulence generation system under both static and dynamic conditions, and comparing to the empty wind tunnel as well, the following key conclusions are drawn:

After the integration of the turbulence generation system, the area of potential flow region in the test section is compressed, and the turbulence intensity is higher than that of the empty wind tunnel. This increase in turbulence is caused by the presence of the turbulence generation system, which enhances the instability of the jet shear layer, thereby intensifying low-frequency fluctuations. Additionally, the vortex shedding pattern at the nozzle is also affected, leading to the formation of three large vortex structures within the shear layer. The complex interactions among these vortices amplify the low-frequency fluctuations, and further reduce the flow quality.

In the dynamic condition of the turbulence generation system with a sinusoidal motion, the spanwise turbulence length scales are significantly larger than the streamwise and vertical scales. Furthermore, the motion of the turbulence generation system notably increases the spanwise turbulence intensity at the bottom of the test section. Regarding the unsteady characteristics of the flow field, the transient flow patterns remain similar to that of the static condition. However, the frequency of dominant velocity fluctuation modes changes, with the 20 Hz velocity fluctuation intensifying while the 40 Hz weakens. In the shear layer under the dynamic condition, the large vortex structures become more irregular. The disturbances caused by the deflectors blur the edges of the vortices, resulting in more random motion, making it difficult to be identified as they move toward the mid-section of the test section. From the pressure field, the motion of the turbulence generation system can slightly disperse the peak frequency of pressure fluctuations while making low-frequency pressure fluctuations more pronounced.

In summary, this active turbulence generation system reconstructs target turbulence conditions in the test section, but also increases the instability of the jet shear layer, leading to heightened low-frequency fluctuations in both velocity and pressure. This in turn affects the turbulence characteristics by the turbulence generation system, and harms the reconstructing accuracy of road aerodynamic conditions. Flow control techniques are worth further investigation in the next step to suppress the resulting extra low-frequency fluctuations.

References

1. McAuliffe, B.R. and D'Auteuil, A., "A System for Simulating Road-Representative Atmospheric Turbulence for Ground Vehicles in a Large Wind Tunnel," *SAE Int. J. Passeng. Cars - Mech. Syst.* 9(1):817-830, 2016, doi:10.4271/2016-01-1624.
2. Vita, G., Hemida, H., Andrianne, T. et al., "Generating Atmospheric Turbulence Using Passive Grids in an Expansion Test Section of a Wind Tunnel," *J. Wind Eng. Ind. Aerodyn.* 178:91-104, 2018, doi: 10.1016/j.jweia.2018.02.007.
3. Neuhaus, L., Hölling, M., Bos, W.J.T. et al., "Generation of Atmospheric Turbulence with Unprecedentedly Large Reynolds Number in a Wind Tunnel," *Phys. Rev. Lett*. 125(15):154503, 2020, doi:10.1103/PhysRevLett.125.154503.
4. Cogotti, A., Cardano, D., Carlino, G. et al., "Aerodynamics and Aeroacoustics of Passenger Cars in a Controlled High Turbulence Flow: Some New Results," SAE Technical Paper 2005-01-1455, 2005, doi:10.4271/2005-01-1455.
5. Cogotti, A., "Update on the Pininfarina Turbulence Generation System and Its Effects on the Car Aerodynamics and Aeroacoustics," SAE Technical Paper 2004-01-0807, 2004, doi:10.4271/2004-01-0807.
6. Carlino, G., Cardano, D., and Cogotti, A., "A New Technique to Measure the Aerodynamic Response of Passenger Cars by a Continuous Flow Yawing," SAE Technical Paper 2007-01-0902, 2007, doi:10.4271/2007-01-0902.
7. Schröck, D., Widdecke, N., and Wiedemann, J., "Aerodynamic Response of a Vehicle Model to Turbulent Wind," 7th FKFS Conference, 2009.
8. Blumrich, R., Widdecke, N., Wiedemann, J. et al., "New FKFS Technology at the Full-Scale Aeroacoustic Wind Tunnel of University of Stuttgart," *SAE Int. J. Passeng. Cars - Mech. Syst*. 8(1):294-305, 2015, doi:10.4271/2015-01-1557.
9. Stoll, D. and Wiedemann, J., "Active Crosswind Generation and Its Effect on the Unsteady Aerodynamic Vehicle Properties Determined in an Open Jet Wind Tunnel," *SAE Int. J. Passeng. Cars - Mech. Syst*. 11(1):429-446, 2018, doi:10.4271/2018-01-0722.
10. Mankowski, O.A., Sims-Williams, D.B., and Dominy, R.G., "A Wind Tunnel Simulation Facility for On-Road Transients," *SAE Int. J. Passeng. Cars - Mech. Syst.* 7(3):1087-1095, 2014, doi:10.4271/2014-01-0587.
11. Amandolèse, X. and Vartanian, C., "Reduction of 3/4 Open Jet Low-Frequency Fluctuations in the S2A Wind Tunnel," *J. Wind Eng. Ind. Aerodyn*. 98(10-11):568-574, 2010, doi: 10.1016/j.jweia.2010.04.011.
12. Künstner, R., Potthoff, J., and Essers, U., "The Aero-Acoustic Wind Tunnel of Stuttgart University," SAE Technical Paper 950625, 1995, doi:10.4271/950625.
13. Holthusen, H. and Kooi, J.W., "Model and Full Scale Investigations of the Low Frequency Vibration Phenomena of the DNW Open Jet," *AGARD Conf. Proc.* 26:1-8, 1997.
14. Soderman, P.T. and Olson, L.E., "The Design of Test-Section Inserts for Higher Speed Aeroacoustic Testing in the Ames 80-by 120-Foot Wind Tunnel," *DGLR/AIAA 14th Aeroacoustics Conf.*, 1992.
15. Bartel, H.W. and McAvoy, J.M., "Cavity Oscillation in Cruise Missile Carrier Aircraft," 1981.
16. Rossiter, J.E., "Wind-Tunnel Experiments on the Flow Over Rectangular Cavities at Subsonic and Transonic Speeds," *Royal Aircraft Establishment*, 1964.
17. Zheng, Z., Wang, Y., and Yang, Z., "Probe into the Method for Calculating Sound Natural Frequency of the Loop of Low-speed Automotive Wind Tunnel," *Noise Vib. Control*. 4:90-93, 2008.
18. Bao, D., "Study on the Flow Mechanism of the Interaction Between Shear Layer and Collector of a 3/4 Open-Jet Wind Tunnel Nozzle," Thesis, Tongji University, 2018.
19. Jia, Q., Huang, L., Zhu, Y. et al., "Experimental Research of Active Control Optimization on a 3/4 Open-Jet Wind Tunnel's Jet Section," *Alexandria Eng. J*. 60(2):2265-2278, 2021, doi:10.1016/j.aej.2020.12.022.
20. Wang, Y., Jia, Q., Xia, C. et al., "Seal Vibrissa-Based Three-Fourths Open-Jet Wind Tunnel Nozzle Optimization," *Proc. Inst. Mech. Eng. Part D: J. Automob. Eng.* 2023, doi:10.1177/09544070231201 20.
21. Wei, H., "Design of Turbulence Generation Device for a 3/4 Open-Jet Wind Tunnel," Thesis, Tongji University, 2023.

Contact Information

*Corresponding author: Huanxia Wei (huanxia.wei@u.nus.edu).

Acknowledgments

This work is supported by National Engineering Research Center of New Energy Vehicles and Power Systems, and Shanghai Key Lab of Vehicle Aerodynamics and Vehicle Thermal Management Systems (23DZ2229029).

Hidden for preprint